Supporting Information

Perepezko et al. 10.1073/pnas.1321518111

SI Text

Alloys and Selected Properties. A listing of the four bulk metallic glass (BMG) alloys studies is given in Table S1 and the differential scanning calorimeter (DSC) traces for the as-cast and annealed Fe-based BMG is shown in Fig. S4.

Hertzian Mechanics. The displaced volume is a function of the penetration depth h and the radius of the indenter R. Hertzian contact mechanics predicts that the indentation depth is related to the amount of load P by (1)

$$P = \frac{4}{3} E_r \sqrt{R h^3}, \quad \text{[S1]}$$

where E_r is the reduced modulus

$$\frac{1}{E_r} = \frac{1-\upsilon_i^2}{E_i} + \frac{1-\upsilon_s^2}{E_s}, \quad \text{[S2]}$$

where E is Young's modulus, ν is the Poisson ratio, and the subscript i refers to the indenter and s to the BMG sample. For the diamond indenter, E_i = 1,141 GPa and ν_i = 0.07. In previous work it has been shown that there is good agreement between the prediction of Eq. **1** and the experimental data before the first pop-in event as shown in Fig. 1. Thus, the transition from perfectly elastic behavior to plastic deformation is associated with the first pop-in event in a nanoindentation measurement. The deformation volume under an indenter increases with the penetration depth of the indenter. The total shearing volume V_d of the first pop-in is the displaced volume under the indenter as given by (1, 2)

$$V_d = \frac{\pi h}{6}\left[3R^2 + h^2\right]. \quad \text{[S3]}$$

The mean contact pressure P_m is

$$P_m = \left(\frac{16 P E_r^2}{9\pi^3 R^2}\right)^{1/3}. \quad \text{[S4]}$$

Finite-Element Analysis and Deformed Volume Evaluation. Even with careful preparation a real sample surface will exhibit some roughness. To assess the influence of surface roughness, ANSYS, a commercial finite-element analysis software, was used to model the 3D nanoindentation in a 2D half-space of finite width by taking advantage of the symmetry of the problem (3). The specimen, assumed to be a cylinder with a diameter of 20 μm and height of 10 μm, was modeled as an elastic solid for a smooth surface and as an elastoplastic solid with isotropic plastic hardening for a rough surface with 100-nm periodic undulations roughness, which is on the scale of the diamond particles used for sample polishing. For a virtual specimen material, the elastic modulus and Poisson's ratio are assumed to be 100 GPa and 0.33, respectively, whereas the yield strength and strain hardening coefficient are set to be 3.0 GPa and 100 MPa, respectively. The rate-dependent plasticity is assumed to follow a Peirce model (3) in which a rate hardening parameter (m) and the material viscosity parameter (γ) are set to 0.01 and $10^{-5}\cdot s^{-1}$, respectively. The contact between the indenter and the specimen surface was modeled using contact elements. The model was meshed by using 6,732 eight-node triangle symmetric elements (PLANE183 and PLANE182) and 201 three-node contact elements (CONTA172 and TARGE169), with a total of 24,383 nodes. Symmetric displacement boundary conditions were applied. Indentation of the sample was simulated by applying a uniform pressure p_z to the line representing the top surface of the indenter, linearly increasing from 0 to $p_{z,\max}$ within a certain period to realize the force-control mode of the experiment.

When plastic deformation is involved, the stress–deformation concentration in the undulations (100 nm in periodicity) will change the distribution of stress and elastic–plastic deformation in the sample. A localized plastic strain in the vicinity of the surface due to undulations will alleviate the possibility of plasticity in the relatively bulk volume underneath the indenter. As a result, the first pop-in that requires a sudden burst of shear deformation in the volume is expected to take place at a smaller indentation load (e.g., 3 mN) than in the case of undulated surface (e.g., ~20 mN), which agrees well with the experimental results.

It is also evident that the surface stress concentrations are not the origin of shear bands because they are too localized to support shear band propagation that is necessary to trigger a pop-in event. Moreover, if surface roughness were operating to promote shear bands the smooth translation of both peaks in the Fe-based BMG after annealing would not have been observed because the sample was repolished after the annealing. Thus, the bimodal distribution signifies that as the indenter penetrates into the sample, it is sampling at least two nucleation sites within the stressed volume.

An initial estimate of V_e can be made by using the displaced volume V_d during indentation using Hertzian contact mechanics. However, because the stress distribution within all regions of the displaced volume does not satisfy the minimum criteria that the stress must be sufficient for both nucleation and propagation, V_e is a fraction of V_d. Based upon the analysis of Packard and Schuh (4) and the finite element method (FEM) results, the volume of the appropriate path that satisfies the minimum criteria is estimated as $V_e \sim 0.01 V_d$.

Analysis of Pop-In Distributions. For the analysis of the distribution of first pop-in events as a function of load it is important to consider the full range of measurements. It is evident from Fig. 2*D* that a distribution with a single peak cannot account for the full range of measurement. To determine whether the measured distribution can be represented by the summation of two or three separate distributions we have conducted a statistical analysis based upon the use of Gaussian distributions (5) (Fig. S6).

Summary of Results from Different BMG Alloys. The results from the BMG alloys not shown in the main text are presented here, along with the analysis of the nucleation rates and nucleation barriers in Figs. S1–S3. The main results are summarized in Table S2. Note that the fits to the experimental cumulative density function are based upon a bimodal distribution analysis. The bimodal fits to the cumulative density function (CDF) are very good in all cases over the entire range of measurement. Because the probability density function (PDF) plots are derived from the experimental CDF, they are sensitive to small variations in the data that can yield variations in the shape of the PDF. The separate contributions from each portion of the bimodal distribution are shown as dashed and dashed–dotted curves.

Nucleation Site Density Evaluation. The complete evaluation of the nucleation rate requires an estimate of β which is the product of an attempt frequency taken as 10^{13} s^{-1} and the number density of sites. Based upon the character of the bimodal distribution of

pop-in events we can derive an independent evaluation of the nucleation site density. For example, for the pop-in distribution for the Cu-based BMG shown in Fig. S2 we note that for the high load pop-ins there are essentially no sites to initiate a low load pop-in. If we consider a Poisson distribution of nucleation sites among the nanoindentation deformed volumes, the fraction of sites without a low load site X is given by $X = 1 - \exp(-mV_d)$, where m = the number of sites per volume and V_d = the deformed volume. For a high load of 24 mN, V_d (high) = 8.73×10^{-21} m^3. For X, we have used 0.1%, which indicates that the fraction of high load sites [i.e., $(1-X)$] is 99.9%. With these values we obtain the following results: m(low) = 9.5×10^{19} m^{-3} and m(high) = 8.5×10^{19} m^{-3}.

We can also check the results for consistency by evaluating the site distribution for low load conditions. For this case with a 12-mN load, V_d(low) = 5.36×10^{-21} m^3. We also assume for simplicity that the site density is not a function of load level. With V_d(low) and the m values determined previously, we find that the low load sites represent 98.6% and the high load fraction is only 1.4%. This indicates that we would rarely see a high load event in the low load range and demonstrates internal consistency.

Simulation Strategy. The activation energies that are found by using the hazard rate and a simple model for nucleation are used to ensure that the values will replicate the datasets that are found by the nanoindentation experiments. These numerical simulations start with an expression for the activation energy and solve for the hazard rate that would result from that energy barrier. For this paper, 10,000 trials were used for each sample. With these starting condition, the following steps break down the way in which pop-ins are recorded:

1) Calculate hazard values for a discrete set of loads (both mechanisms).
2) Use an initial value for the overall sampling fraction for the mechanisms (i.e., how many of the observed pop-ins "belong" to mechanism 1 or mechanism 2).
3) Start the trials (increased number of trials gives lower sampling error).
   a) Compare a test variable ($0 \le R_1 \le 1$) to the sampling fraction to decide mechanism.
      i) Create a random test variable ($0 \le R_{2,i} \le 1$) for each load.
      ii) Compare the hazard experienced at each load to the corresponding $R_{2,i}$.
      iii) Stop the test at the first instance where the hazard is greater than $R_{2,i}$.
      iv) Record the load at which pop-in occurs and the mechanism used when the hazard is greater than $R_{2,i}$.
      v) Start again at 3a).
4) Refine step 2 estimate and proceed to step 3a).

1. Chen MW (2008) Mechanical behavior of metallic glasses: Microscopic understanding of strength and ductility. *Annu Rev Mater Res* 38:445–469.
2. Bei H, Lu ZP, George EP (2004) Theoretical strength and the onset of plasticity in bulk metallic glasses investigated by nanoindentation with a spherical indenter. *Phys Rev Lett* 93(12):125504.
3. ANSYS (2007) Documentation for ANSYS, release 11.0 (ANSYS Inc., Canonsburg, PA).
4. Packard CE, Schuh CA (2007) Initiation of shear bands near a stress concentration in metallic glass. *Acta Mater* 55(6):5348–5358.
5. Cameron CA, Windmeijer FAG (1997) An R-squared measure of goodness of fit for some common nonlinear regression models. *J Econom* 77(2):329–342.

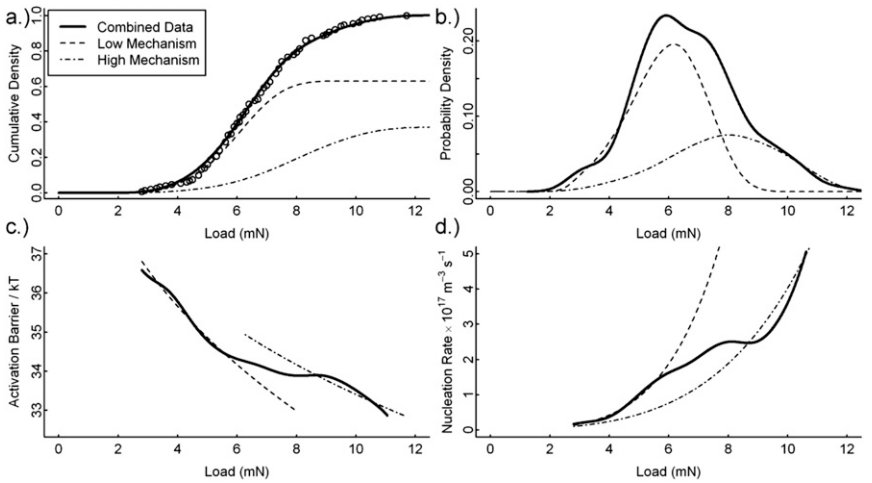

Fig. S1. The activation energy barrier and nucleation rates of the first pop-ins in the Au-BMG samples. (*A*) The experimental cumulative density function is displayed together with the separate calculated contributions from each of the two nucleation sites. There is a close agreement between the fitted cumulative distribution and the measurements over the entire range including the endpoints. (*B*) The experimental probability density function is displayed together with the separate calculated contributions from each of the two nucleation sites. There is a close agreement between the fitted probability distribution and the measurements over the entire range including the endpoints. (*C*) The trend of activation barrier and (*D*) the resultant nucleation rates as a function of load are separated and indicate the existence of two nucleation sites with an overlapping load range of operation. In the low load range where the nucleation barrier ranges from 36*kT* to 34*kT*, the nucleation rate (*D*) reaches 1.5×10^{17} m^{-3}s^{-1} when a transition occurs to operation of the high load site.

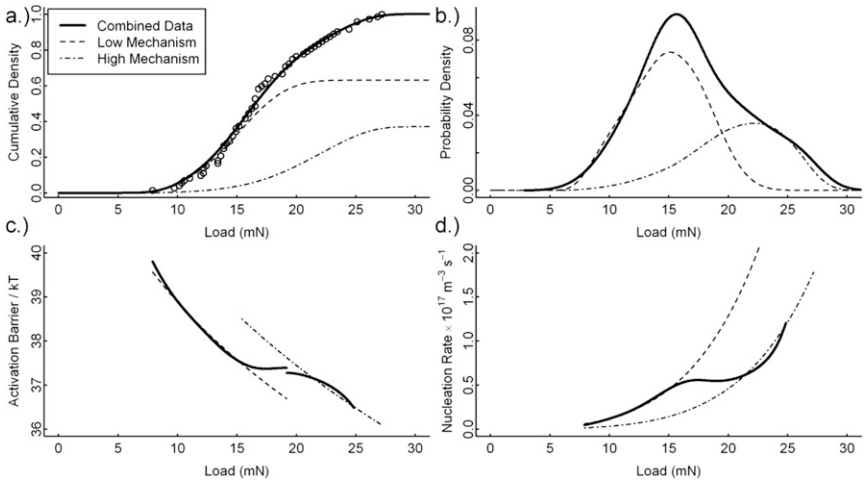

Fig. S2. The activation energy barrier and nucleation rates of the first pop-ins in the Cu-BMG samples. (*A*) The experimental cumulative density function is displayed together with the separate calculated contributions from each of the two nucleation sites. There is a close agreement between the fitted cumulative distribution and the measurements over the entire range including the endpoints. (*B*) The experimental probability density function is displayed together with the separate calculated contributions from each of the two nucleation sites. There is a close agreement between the fitted probability distribution and the measurements over the entire range including the endpoints. (*C*) The trend of activation barrier and (*D*) the resultant nucleation rates as a function of load are separated and indicate the existence of two nucleation sites with an overlapping load range of operation. In the low load range where the nucleation barrier ranges from 39*kT* to 37.4*kT*, the nucleation rate (*D*) reaches 0.5×10^{17} $m^{-3}s^{-1}$ when a transition occurs to operation of the high load site.

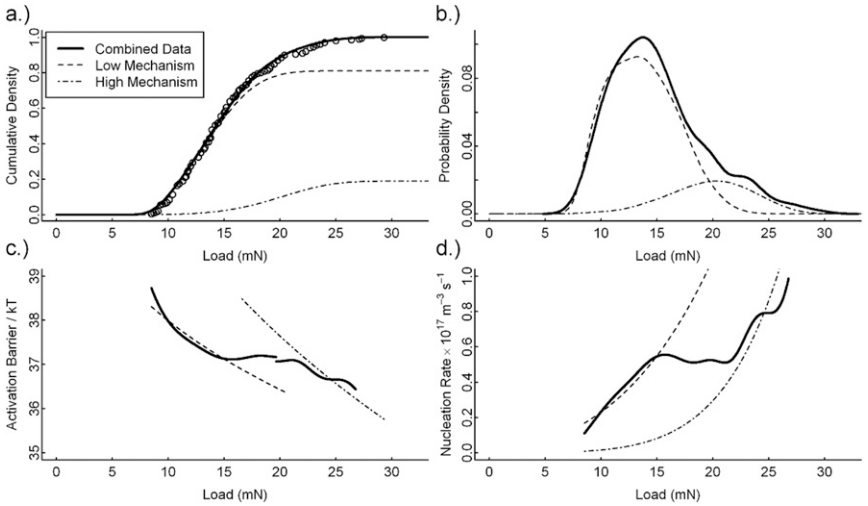

Fig. S3. The activation energy barrier and nucleation rates of the first pop-ins in the Zr-BMG samples. (*A*) The experimental cumulative density function is displayed together with the separate calculated contributions from each of the two nucleation sites. There is a close agreement between the fitted cumulative distribution and the measurements over the entire range including the endpoints. (*B*) The experimental probability density function is displayed together with the separate calculated contributions from each of the two nucleation sites. There is a close agreement between the fitted probability distribution and the measurements over the entire range including the endpoints. (*C*) The trend of activation barrier and (*D*) the resultant nucleation rates as a function of load are separated and indicate the existence of two nucleation sites with an overlapping load range of operation. In the low load range where the nucleation barrier ranges from 38*kT* to 37*kT*, the nucleation rate (*D*) reaches 0.5×10^{17} $m^{-3}s^{-1}$ when a transition occurs to operation of the high load site.

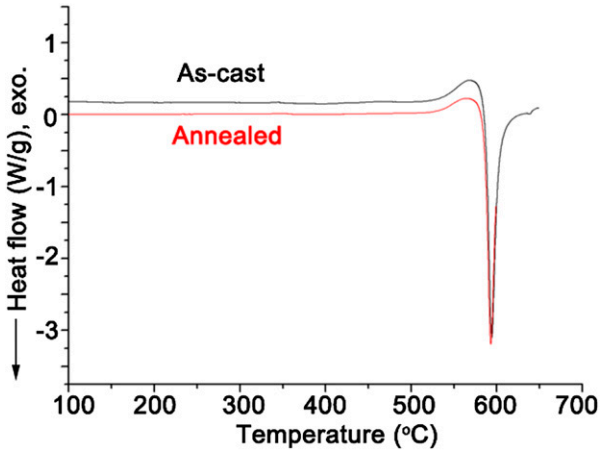

Fig. S4. DSC heating (40 °C/min) results for as-cast and annealed (heated to 540 °C and reheated) $Fe_{57.6}Co_{14.4}B_{19.2}Si_{4.8}Nb_4$ amorphous sample.

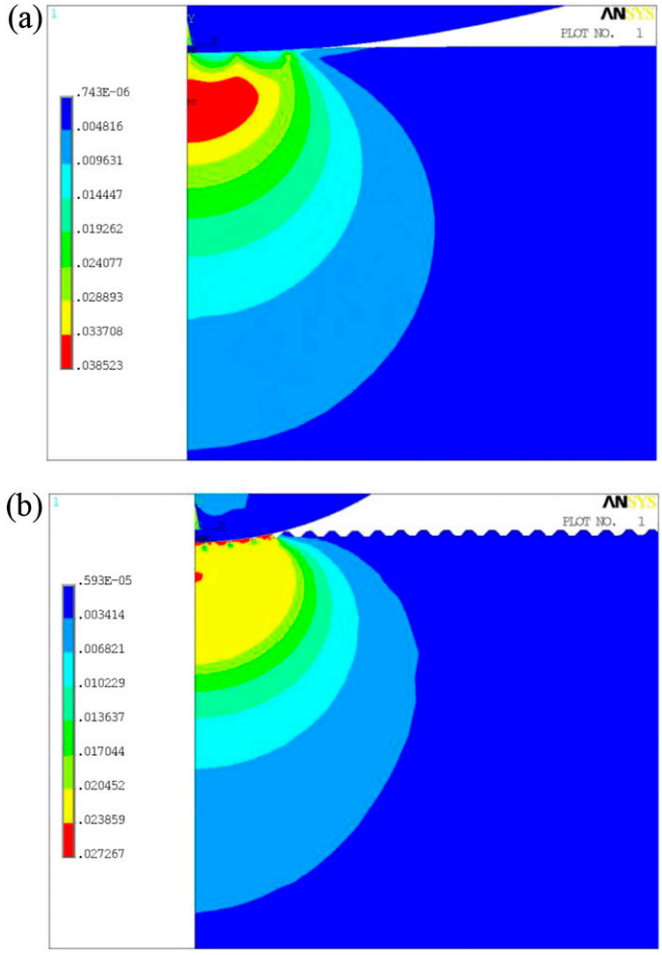

Fig. S5. (*A*) FEM results on the von Mises strain ($P = 2$ mN) for the elastic indentation deformation of a smooth surface. (*B*) FEM results on the von Mises strain ($P = 20$ mN) for the elastoplastic indentation deformation of a surface with 100-nm undulations.

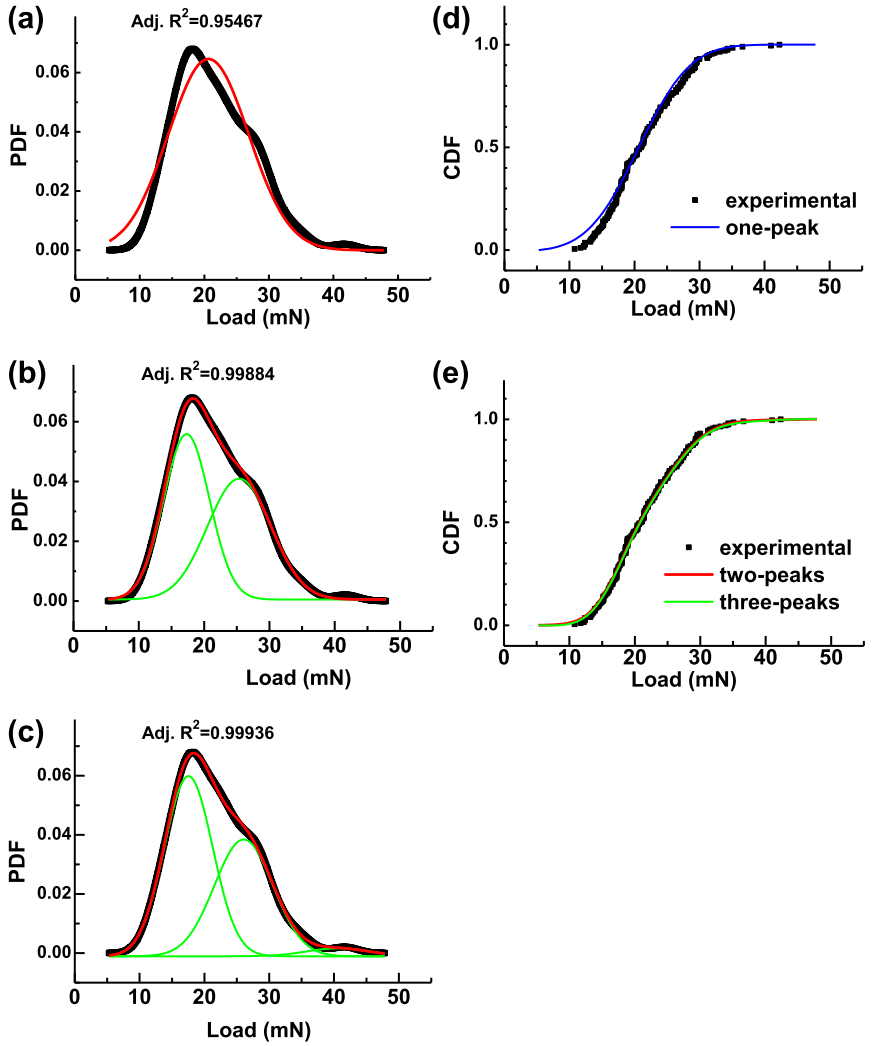

Fig. S6. Group of plots compares the fitting by one-, two-, and three-peak functions. The black curves are the kernel density of the experimental data for the as-cast Fe-based BMG. The red curves are fits composed of (*A*) one, (*B*) two, or (*C*) three peak functions. The green curves are decomposed single peaks from the multimodal functions. The fitting results can be evaluated by statistical parameters such as the coefficient of determination, R^2. A large adjusted R^2 (closer to 1) indicates a good model fit (5). The plots confirm that the two-peak function gives much better fitting than a single-peak function according to the values of adjusted R^2 (increase from 0.95467 to 0.99884 for as-cast sample). However, adding one more peak to the fitting function does not change the fit very much according to the values of adjusted R^2 (increase from 0.99884 to 0.99936). Moreover, the resulting fits to the experimental data-based CDF plots also show that (*D*) a single-peak function does not provide a satisfactory fit over the entire measurement range, but (*E*) a two-peak function provides a very good fit. The addition of a third peak does not improve the fit. Similar results are obtained for the other BMG samples. Therefore, we use a bimodal fitting function containing two peaks to analyze the experimental results.

Table S1. List of alloys and some selected properties

Alloy (at. %)	σ, GPa	ε, %	E, GPa	ν	G, GPa	T_g, K	T/T_g
$Fe_{57.6}Co_{14.4}B_{19.2}Si_{4.8}Nb_4$	4.05	2.0	203	0.32	76.9	807	0.37
$Cu_{60}Hf_{25}Ti_{15}$	2.01	1.7	124	0.36	45.6	740	0.40
$Au_{49.5}Ag_{5.5}Pd_{2.3}Cu_{26.9}Si_{16.3}$	1.20	—	74.4	0.406	26.5	405	0.74
$Zr_{55}Cu_{25}Ni_{10}Al_{10}$	1.90	2.2	86	0.36	31.6	685	0.43

Table S2. Summary of shear band nucleation analysis results

BMG	$W(\tau)_L^*/kT$ (load range, mN)	J_L ($10^{17}m^{-3}s^{-1}$) (load range, mN)	Site density (low load, m^{-3})	$W(\tau)_H^*/kT$ (load range, mN)	J_{hH} ($10^{17}m^{-3}s^{-1}$) (load range, mN)	Site density (high load, m^{-3})
$Fe_{57.6}Co_{14.4}B_{19.2}Si_{4.8}Nb_4$ (as-cast)	39.5–38 (11–16)	0.08–0.2 (11–16)	1×10^{20}	37.5–36.5 (28–31)	0.5–1.0 (28–31)	9.1×10^{19}
$Fe_{57.6}Co_{14.4}B_{19.2}Si_{4.8}Nb_4$ (annealed)	39–38 (10–17)	0.01–0.3 (10–17)	1×10^{20}	38–37 (29–39)	0.5–1.0 (29-39)	9.2×10^{19}
$Cu_{60}Hf_{25}Ti_{15}$	39–37.5 (6–15)	0.05–0.5 (6–15)	9.5×10^{19}	37–36.5 (21–25)	0.5–1.0 (21–25)	8.5×10^{19}
$Au_{49.5}Ag_{5.5}Pd_{2.3}Cu_{26.9}Si_{16.3}$	36–34 (3–6)	0.02–1.5 (3–6)	1.3×10^{19}	34–33 (8–11)	2.5–5.0 (8–11)	1.3×10^{19}
$Zr_{55}Cu_{25}Ni_{10}Al_{10}$	38–37 (9–15)	0.1–0.5 (9–15)	7.3×10^{19}	37.25–36.25 (21–26)	0.5–1 (22–27)	6.6×10^{19}